Proceedings of IMECE2007
2007 ASME International Mechanical Engineering Congress and Exposition
November 11-15, 2007, Seattle, Washington, USA

IMECE2007-43156

NON-SPHERICAL COLLAPSE OF AN AIR BUBBLE SUBJECTED TO A LITHOTRIPTER PULSE

Eric Johnsen*
Division of Engineering and Applied Science
California Institute of Technology
Pasadena, California 91125
ejohnsen@caltech.edu

Tim Colonius
Division of Engineering and Applied Science
California Institute of Technology
Pasadena, California 91125
colonius@caltech.edu

Wayne Kreider
Center for Industrial and Medical Ultrasound
Applied Physics Laboratory
University of Washington
Seattle, Washington 98105
wkreider@u.washington.edu

Michael R. Bailey
Center for Industrial and Medical Ultrasound
Applied Physics Laboratory
University of Washington
Seattle, Washington 98105
bailey@apl.washington.edu

ABSTRACT

In order to better understand the contribution of bubble collapse to stone comminution in shockwave lithotripsy, the shock-induced and Rayleigh collapse of a spherical air bubble is investigated using numerical simulations, and the free-field collapse of a cavitation bubble is studied experimentally. In shock-induced collapse near a wall, it is found that the presence of the bubble greatly amplifies the pressure recorded at the stone surface; the functional dependence of the wall pressure on the initial stand-off distance and the amplitude are presented. In Rayleigh collapse near a solid surface, the proximity of the wall retards the flow and leads to a more prominent jet. Experiments show that re-entrant jets form in the collapse of cavitation bubbles excited by lithotripter shockwaves in a fashion comparable to previous studies of collapse near a solid surface.

NOMENCLATURE

R_o Initial bubble radius
H Initial stand-off from the wall
P Pulse amplitude
M Mach number
σ Pulse width
ρ Density
$\mathbf{u}$ Velocity vector
p Pressure
E Total energy
γ Ratio of specific heats (for gases)
P_∞ Stiffness constant
c Sound speed
v_j Maximum jet speed
v_o Maximum speed of distal side

INTRODUCTION

Shockwave lithotripsy (SWL) is the most common treatment for kidney stones [1]. The main advantage of this procedure consists in avoiding surgery altogether by generating shockwaves extracorporeally and focusing them onto kidney stones [2]. As a result, the stones are broken into fragments small enough that they can be passed naturally by the human body.

*Address all correspondence to this author.

Because of the complex physics governing the process, the stone comminution mechanism is not yet fully understood. Lithotripter pulses consist of a steep compressive front followed by a long expansion tail with a tensile component. Since kidney stones are typically immersed in urine, this tension enhances the formation and growth of bubbles near the stone. Consequently, two mechanisms bear important roles in stone comminution: spallation due to stress waves reflected within the stone [3, 4], and cavitation erosion due to violent bubble collapse along the stone surface [5, 6]. It has been proposed that the combined effect of the internal stress waves and of cavitation erosion pulverizes the stones [4]. More recently, it has been observed that the interference of shear waves generated by the passage of the pulse along the stone may play an important role [7].

The impact of bubble dynamics on stone comminution is still unclear. After the passage of a lithotripter pulse, bubbles generally gather in clusters that grow and collapse near the stone surface, thereby generating shockwaves [8, 9]. In order to provide an estimate for cavitation damage, the collapse of a single bubble near a wall is considered. In SWL, single bubble collapse near the stone takes place on two time scales: a short one, where the collapse is induced by the passage of the pulse (shock-induced collapse $\sim 1\mu$s), and a long one, where the bubble grows to a large size due to cavitation induced by the tensile part of the pulse and subsequently collapses (Rayleigh collapse $\sim 200\mu$s). When a bubble collapses near a solid surface, a re-entrant jet directed towards the surface forms and penetrates the bubble [10]. The impact of the jet onto the stone leads to pitting and has been regarded as the primary cause of cavitation erosion in SWL [5,6]. Re-entrant jets also form when bubbles are impacted by shockwaves, even when far from solid surfaces [11–13].

In the present study, a high-order accurate, quasi-conservative, shock- and interface-capturing scheme [14] is used to simulate both shock-induced and Rayleigh collapse near a solid surface. A detailed presentation of the problem is provided in Section 1, while the numerical model is briefly described in Section 2. Preliminary results from shock-induced and Rayleigh collapse are presented and discussed in Section 3, along with experiments on the collapse of a cavitation bubble. Finally, the findings are summarized in Section 4.

1 COMPUTATIONAL SET-UP

A spherical air bubble of radius, R_o, in water is in equilibrium with its surroundings and located at some distance, H, from a rigid wall, which represents the kidney stone. The computational domain consists of a cylinder, along whose centerline the bubble is located; azimuthal symmetry is assumed, so that the computation is axisymmetric. A slice through the center is depicted in Figure 1, where the dashed line denotes the domain. A lithotripter pulse of amplitude, P, and width, σ, starts on the right of the bubble and propagates at normal incidence towards the wall. Reflecting and symmetry boundary conditions are used along the centerline and the wall, while incoming and non-reflecting boundary conditions are specified along the right and about the circumference of the domain. The wall along the left side is removed for Rayleigh collapse in a free field.

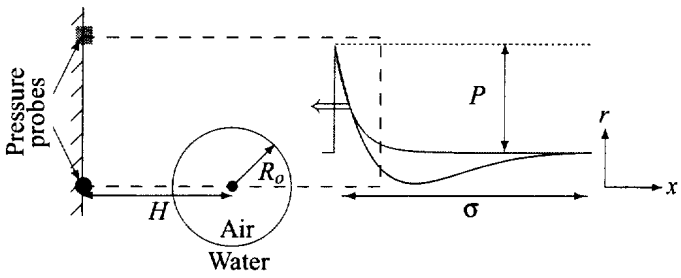

Figure 1. Schematic of the problem.

Because the kidney stone is located at the the focus of a lithotripter, the waveform is approximately planar and consists of a steep compression, followed by a long expansion with a tensile part, as modelled by Church [15]. The amplitude of the initial compression is typically $P = 35$ MPa, while the tension reaches -10 MPa. The width of the pulse is approximately $\sigma = 6.75$mm. The properties of waveform are chosen to represent those observed at the focus of the Dornier HM3 clone used for the experiments in Section 3.3. Because the present numerical model does not include cavitation, an exponential waveform, which remains positive, is used, as shown in Figure 1; thus, the pulse consists of a shock followed by an expansion that closely matches the decay of the lithotripter profile. The width at half-maximum is 0.35mm and matches that of the Church profile. This assumption is valid for studying shock-induced collapse, since the width of the pulse is much larger than the bubble radius; the collapse time of the bubble is much smaller than the characteristic time of wave propagation, so that the tensile part of the pulse has not yet entered the domain. As a measure of damage, the wall pressure is recorded at the top and center of the domain, as shown in Figure 1.

The non-dimensionalization is performed using the initial density, ρ_L, and speed of sound, c_L, of the water, and the initial bubble radius, R_o. For the present study, $R_o = 50\mu$m. The geometrical properties are listed in Table 1. In non-dimensional units, the length and radius of the domain, are 5 and 2.5 for shock-induced collapse and 8 and 8 for Rayleigh collapse. Following the analysis of [16], the water properties are $\gamma_L = 6.59$ and $P_\infty = 3982$atm, $\rho_L = 998$kg/m^3 and $c_L = 1647$m/s. The density of the gas is $\rho_G = 1.22$kg/m^3.

Table 1. Geometrical properties.

Dimensional value	Non-dimensional value
$H = 55 - 170\mu$m	$H/R_o = 1.05 - 3.4$
$\sigma = 6.75$mm	$\sigma/R_o = 135$
$P = 70.7 - 568$atm	$P/P_o = 70.7 - 568$ ($M_s = 1.005 - 1.040$)

2 NUMERICAL MODEL

The numerical simulation of compressible multiphase flows is notoriously challenging. Interfaces separating fluids whose density ratio is high (1000 : 1) must be tracked and can undergo large non-spherical deformations. In the problem of interest, the main flow physics are governed by interactions between various types of waves and interfaces. Thus, to a first approximation, compressible multicomponent flows are considered, where the fluid components are assumed immiscible. Viscous and thermal diffusion are ignored, and surface tension and phase change effects are neglected. The Euler equations govern such flows,

$$\mathbf{q}_t + \nabla \cdot \mathbf{f}(\mathbf{q}) = \mathbf{0}, \quad \mathbf{q} = \begin{pmatrix} \rho \\ \rho \mathbf{u} \\ E \end{pmatrix}, \quad \mathbf{f} = \begin{pmatrix} \rho \mathbf{u} \\ \rho \mathbf{u}\mathbf{u} + p\mathbf{I} \\ (E+p)\mathbf{u} \end{pmatrix}, \quad (1)$$

where $\mathbf{I}$ is the identity tensor. Cylindrical coordinates with azimuthal symmetry are used for this particular geometry. The system is closed using a stiffened equation of state [17],

$$\frac{1}{\gamma - 1} p + \frac{\gamma}{\gamma - 1} P_\infty = E - \frac{1}{2} \rho \mathbf{u} \cdot \mathbf{u}. \quad (2)$$

For perfect gases, γ is the ratio of specific heats and $P_\infty = 0$; for water, γ and P_∞ are determined from Hugoniot data [16]. In this formulation, interfaces can be represented by a discontinuity in the properties, γ and P_∞. Thus, the functions, $\boldsymbol{\phi} = (1/(\gamma - 1), \gamma P_\infty/(\gamma - 1))^T$, obey the advection equation,

$$\boldsymbol{\phi}_t + \mathbf{u} \cdot \nabla \boldsymbol{\phi} = \mathbf{0}. \quad (3)$$

The system of equations (1) and (3) is solved by extending the high-order accurate quasi-conservative shock- and interface-capturing scheme developed by Johnsen and Colonius [14] to cylindrical coordinates with azimuthal symmetry. The reader is referred to [14] for more details on the numerical method.

Because of difficulties in the treatment of shockwaves in compressible multiphase flows, few computational studies of bubble collapse have been undertaken. Ding and Gracewski [18] used an Arbitrary Lagrangian-Eulerian method with artificial viscosity to simulate the interaction between a bubble and a shockwave; contrary to comparable experiments [12], jetting was not observed for shockwaves of 30 MPa. Ball *et al.* [19] employed a two-dimensional Free-Lagrange method to study the response of a gas cylinder subjected to strong shockwaves in water; results captured the main features of prior experiments [20], though the implementation of the method is rather complicated. Klaseboer *et al.* [21] used a Boundary-Element method (BEM) to simulate the response of a bubble to a strong top-hat pressure pulse; however, because it is based on incompressible flow, BEM does not adequately represent shockwaves.

3 RESULTS AND DISCUSSION

3.1 Shock-induced collapse

To understand the bubble dynamics occurring in SWL, shock-induced collapse is first considered, where a bubble is subjected to a lithotripter pulse. This problem occurs on a short time scale, as the bubble collapses due to the passage of the shock. A qualitative description of the events occurring for the case, $P/P_o = 357$, $H/R_o = 2.5$, is shown in Figure 2. Slices across the computational domain through the centerline show numerical Schlieren [22] and pressure contours, with the interface outlined in black in the pressure plot. The wall is denoted by the gray area on the left side of each frame. The computational grid has 800×400 points.

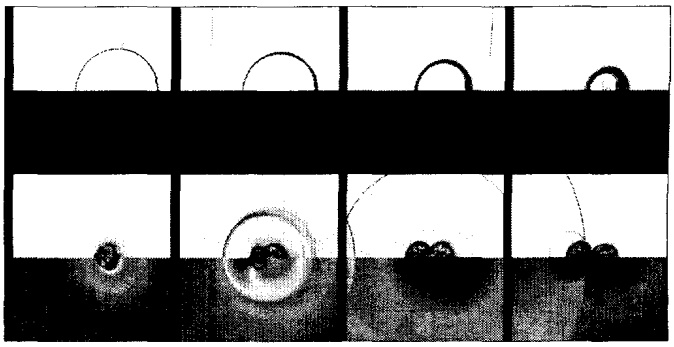

Figure 2. Numerical Schlieren (top) and pressure (bottom) contours for shock-induced collapse; $H/R_o = 2.5$, $\sigma/R_o = 135$, $P/P_o = 357$.

When the left-moving lithotripter pulse hits the bubble, an expansion wave is reflected because of the impedance mismatch between water and air, while a weak shockwave is transmitted into the bubble (frame 1); baroclinic vorticity is generated along the interface due to the misalignment of the pressure and density gradients. The pulse is then reflected off the wall, as the bubble starts to collapse non-spherically (frames 2-4). This departure from the initially spherical shape is attributed to two factors: acceleration of the far side of the bubble towards the wall [23] and baroclinic torque [24]. When the jet hits the distal side of the

bubble (frame 5), a large water-hammer pressure is generated and propagates radially outwards (frame 6). It is then reflected off the wall back onto the bubble (frame 7). After the occurrence of the water-hammer, the bubble becomes a vortex ring [25], which rebounds as it convects towards the wall; in the meantime, pressure waves are reflected between the bubble and the wall (frames 8). In this specific case, the bubble does not hit the wall during the computation time.

The history of the wall pressure at the center and at the top of the wall are shown in Figure 3. First, the lithotripter pulse hits the wall. The smaller and slightly delayed amplitude measured at the center shows that the bubble shields the wall to a certain extent, though the diffracted pressure due to the incoming shock still reaches this point eventually. The pressure doubles as the pulse reflects off the wall, as illustrated by the value of P plotted in the figure. The much larger pressure due to the bubble collapse is then observed; even at the top of the domain (located at 2.5 initial radii of the centerline), this pressure is far greater than the initial lithotripter pulse. Further pressure peaks occur due to wave reflections of the water-hammer pulse between the wall and the bubble interface; in addition, the first rebound generates a pressure of significant amplitude.

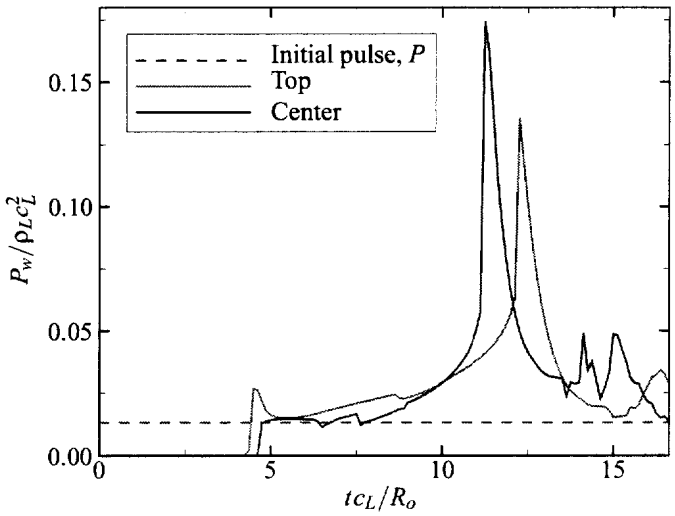

Figure 3. History of the wall pressure at the center (solid red) and top (solid green) of the domain for shock-induced collapse, with the value of the initial pulse (dashed blue).

The history of the bubble volume and centroid position are shown in Figure 4. As expected, the bubble collapses to a very small size and subsequently rebounds to a size much smaller than its initial size, losing energy mostly by acoustic radiation [26]. When it reaches its minimum size, the bubble accelerates towards the wall, as the tighter vortex ring convects towards the wall. When the bubble expands, the size of the vortex ring grows, thus decreasing the convective speed.

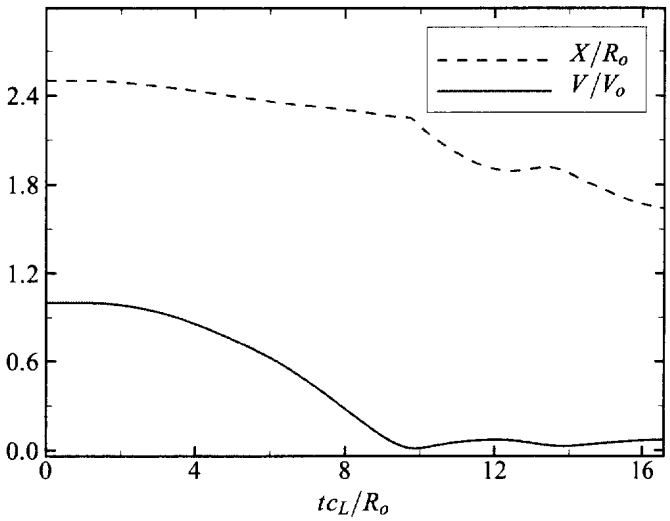

Figure 4. History of the bubble volume and position for shock-induced collapse.

The computations show that two essentially simultaneous events occur when the maximum pressure is measured: the water-hammer pressure and the minimum volume of the bubble. Based on the present temporal and spatial resolutions, it is currently not possible to distinguish between the two events. As shown in Figure 5, the jet reaches a speed of nearly 350 m/s, while the distal side moves at a speed of about 400 m/s. The water hammer equation,

$$P_{wh} = \rho_L c_L v_j \frac{\rho_S c_S}{\rho_S c_S + \rho_L c_L}, \tag{4}$$

can be used to compute the pressure along a solid wall of density, ρ_S, and speed of sound, c_S, impacted by a liquid jet of speed, v_j. In the present case, the "wall" is in fact liquid, and the relevant jet speed is the relative speed of the jet and the distal side, v_o (see Figure 12). The pressure at the tip of the jet measured at the instant of impact is 866 MPa, while the water-hammer contribution is 778 MPa. However, a much larger pressure of 2.37 GPa is measured at a neighboring location, which is perhaps also due to the compression of the gas in the bubble.

The dynamics of the axisymmetric problem are different from those of a corresponding two-dimensional case [27]. The collapse is more rapid here, due to the geometry. As a reminder, diffusion, surface tension, and phase change effects have been neglected. Diffusion and phase change would slow down the

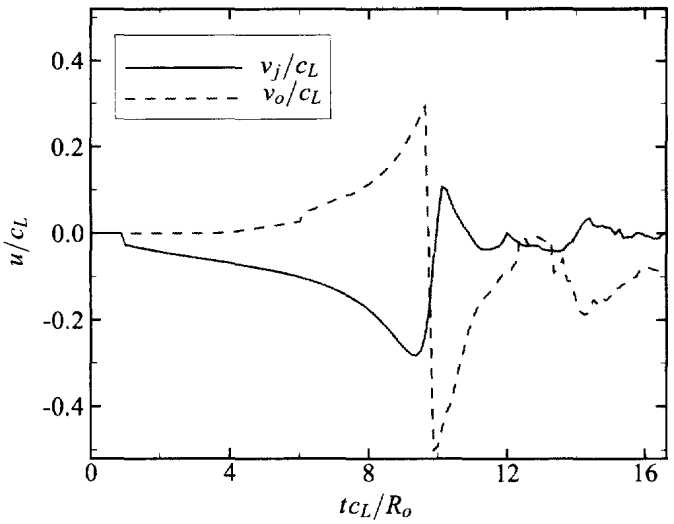

Figure 5. History of the jet speed and the speed of the distal side for shock-induced collapse.

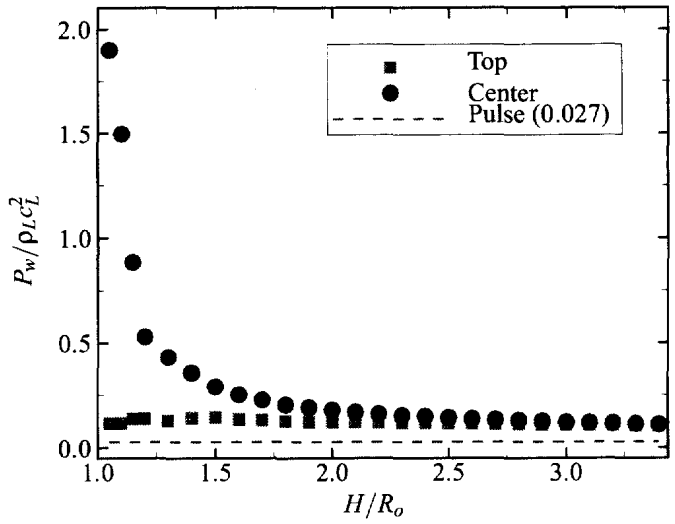

Figure 6. Maximum wall pressure as a function of the initial stand-off distance form the wall for shock-induced collapse.

bubble collapse, while surface tension would attenuate the formation of the jet. Except during the final stages of collapse, these effects are expected to be secondary (*i.e.*, *Re* and *We* are large), such that the overall behavior is still captured adequately by the present simulations. Further studies will include these effects and consider the effect of varying the pulse width, σ, and the initial bubble radius.

3.1.1 Effect of the initial stand-off distance To study the effect of the initial stand-off distance from the wall, $\sigma/R_o = 135$ and $M = 1.025$ (or $P/P_o = 357$) are held constant, while H/R_o is varied; the value, $H/R_o = 2.5$, corresponds to the base problem of Table 1. Figure 6 shows the maximum wall pressure due to the bubble collapse and pulse, and jet speed as a function of the initial stand-off distance, H/R_o.

The pressure at the center of the wall is large for small distances, since the water-hammer impact occurs close to the wall. At the top, the pressure is almost constant, because the pressure pulse is propagating radially outwards, so that the distance from the location of the water-hammer to the top of the domain does not vary significantly with H/R_o. For large enough H/R_o, the pressure at the center tends to the value of that at the top, thus illustrating that the pressure wave becomes planar if the collapse occurs far enough from the wall. Still, the pressure due to the bubble collapse is much larger than that of the pulse for the range of H/R_o considered here. This shows that even bubbles collapsing some distance away from the stone may contribute to erosion.

3.1.2 Effect of the pulse amplitude To study the effect of the pulse amplitude, $H/R_o = 2.5$ and $\sigma/R_o = 135$ are held constant, while M is varied; the value, $M = 1.025$ (or $P/P_o = 357$), corresponds to the base problem of Table 1. Figure 7 shows the wall pressure as a function of the Mach number of the pulse for the incoming shock and that due to the bubble collapse, at the center and at the top of the domain. Only values of $M \gtrsim 1$ are considered (*i.e.*, weak shocks), as these are representative of SWL.

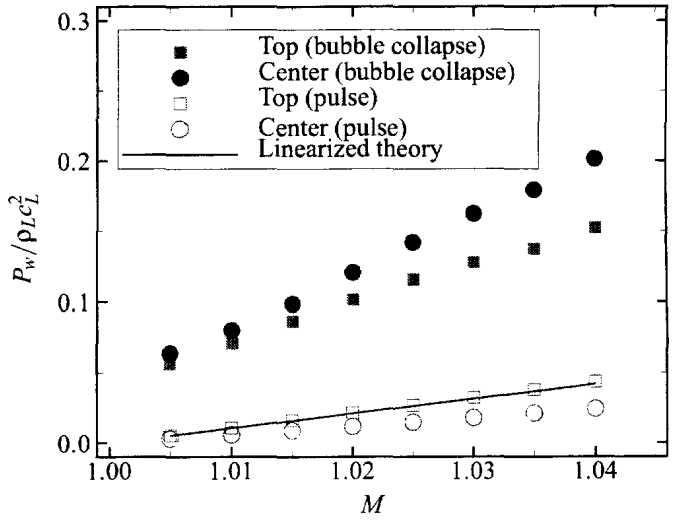

Figure 7. Maximum wall pressure as a function of the pulse Mach number for shock-induced collapse.

The wall pressure increases linearly with the Mach number, but at different rates depending on the quantity measured. At the

top of the domain, the wall feels the full effect of the incoming lithotripter pulse, which is then reflected so that the wall pressure is twice that of the incoming pulse. From the normal shock relations for the stiffened equation of state, the pressure is related to the Mach number, γ and P_∞ as follows [16]:

$$\frac{P}{P_o} = 1 + \frac{2\gamma}{\gamma+1}\left(1 + \frac{P_\infty}{P_o}\right)(M^2 - 1). \quad (5)$$

Thus, $M = 1.005$ corresponds to $P/P_o = 70.3$ and $M = 1.040$ to $P/P_o = 565$. For Mach numbers close to unity, this expression can be linearized to yield

$$\frac{P}{\rho_L c_L^2} = \frac{P_o}{\rho_L c_L^2} + \frac{2\gamma}{\gamma+1}\left(\frac{P_o}{\rho_L c_L^2} + \frac{P_\infty}{\rho_L c_L^2}\right) 2x + O(x^2), \quad (6)$$

where $M = 1 + x$ and $0 < x \ll 1$. The wall pressure due to the pulse is obtained by doubling this value. Using the parameters of Table 1, $P_w \approx 1.05x$, which is the solid line shown in Figure 7. The computed data matches this line very well; a least squares fit of the data yields a line of slope, 1.09. The wall pressure due to the lithotripter pulse is smaller at the center than at the top of the domain, because the bubble "shields" the wall from the pulse. In addition, its rate of increase is also smaller. On the other hand, the wall pressure due to the bubble collapse is greater at the center than at the top of the domain, as previously discussed. The jet speeds measured here are comparable to those of Ohl and Ikink [12]; they are somewhat larger, because the maximum speed is considered and because the bubble is located near the wall.

The dependence on the pulse amplitude can be useful when considering shock propagation through a cloud of bubbles near a solid surface. As the shock propagates through the cloud, it becomes attenuated, such that the bubbles nearest to the wall only feel a fraction of the original pressure ratio. Using a model for shock propagation through bubbly mixtures [28] to provide the attenuation of the pulse as a function of void fraction and position within the cloud, the potential damage generated by the bubbles at the edge of the cloud could be estimated using Figure 7.

3.2 Rayleigh collapse

In order to better understand the implications of the reentrant jet on the bubble collapse, preliminary results on Rayleigh collapse in a free field and near a wall are presented in this section. In this problem, the bubble is initially in equilibrium with its surroundings at some ambient pressure, P_o; then the pressure of the surrounding liquid is instantaneously raised to some pressure, P, thus causing the bubble to collapse [29]. The pressure ratio, P/P_o, can be related to that of a shock passing over a bubble. This problem has been designed to make comparisons to shock-induced collapse, so that similar parameters are chosen. In the context of SWL, bubbles grow to a very large size (at which point the initial conditions are similar to that of Rayleigh collapse) before collapsing, so that the time scale is much longer than that of the shock-induced collapse considered in the previous section. Such collapses are investigated experimentally in this effort (see Section 3.3) and will be considered numerically in a later study.

3.2.1 Rayleigh collapse in a free field As a reference case, Rayleigh collapse in a free-field is first considered. Figure 8 shows numerical Schlieren and pressure contours for the case, $P/P_o = 357$, with the interface outlined in black in the pressure plots. This pressure corresponds to a shock Mach number of 1.025. The computational domain has 800×800 points.

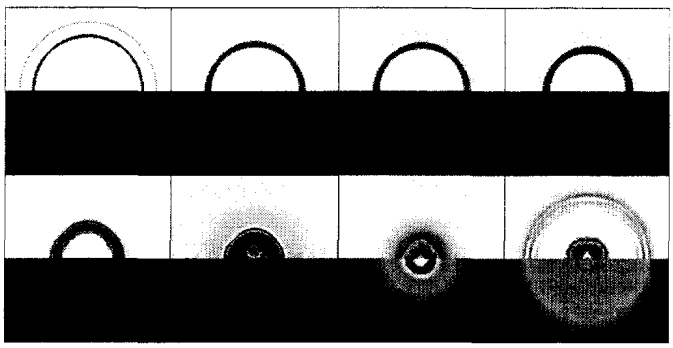

Figure 8. Numerical Schlieren and pressure contours of Rayleigh collapse in a free field, with $P/P_o = 357$.

In frame 1, the expansion wave released due to the initial Riemann problem at the bubble interface propagates radially outwards, while a shock propagates within the bubble, though its amplitude is too small to be seen initially. The shock is visible in frame 2 as it focuses, converges to the center of the bubble in frame 3 and propagates back outwards in frame 4. During this time, the bubble is collapsing, such that the shock hits the bubble interface in frame 5; Richtmyer-Meshkov instability resulting from this phenomenon does not appear to be an important effect. The interface accelerates significantly in frame 6, where radiating acoustic waves are visible. The interface starts to go unstable just before frame 7 due to the change of sign of its acceleration, suggesting that Rayleigh-Taylor instability is the driving instability [30]; this phenomenon has been observed in experiments [31]. The bubble reaches its minimum volume in frame 7, generating a shock due to the high compression of the gas within the bubble [32] that propagates radially outwards (frame 8). At this stage, the interface is greatly perturbed, such that the bubble is no longer spherical. It should be recalled that surface tension,

which acts as a stabilizing force, is neglected.

Figure 9 shows the history of the bubble volume for different resolutions, N, where the grid has $N \times N$ points. The dashed line denotes the numerical solution to the Gilmore equation [33], which is a modified Rayleigh-Plesset equation that takes into account liquid compressibility. However, it is only valid to order M^2, where the Mach number is defined as the speed of interface divided by the local sound speed. This approximation is not a good one for the pressure ratios considered in this study, but gives an estimate of the history of the bubble volume. Since the computation is fully compressible, the computed solution is expected to be slower than the Gilmore solution. Furthermore, the bubble does not remain spherical in the computation, and the pressure within the bubble is not uniform. Nevertheless, the computation initially agrees with the Gilmore equation, as M is still small.

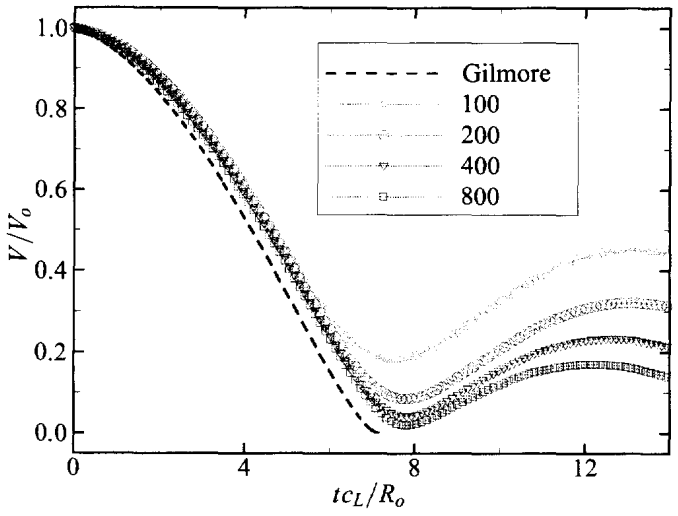

Figure 9. History of the bubble volume for different resolutions for Rayleigh collapse in a free field.

Figure 9 shows that the computed solution converges. However, a finer grid is required to generate quantitative results. Increasing the number of grid points decreases the effect of the numerical diffusion, which damps the process in a fashion similar to the physical viscosity. The code is currently being extended such that the grid can be stretched and higher resolution can be achieved; the present results should therefore be considered in a qualitative sense.

3.2.2 Rayleigh collapse near a wall When a bubble collapses near a solid wall, a re-entrant jet, directed towards the surface, forms and penetrates the bubble [10]. Figure 10 shows numerical Schlieren and pressure contours for the case, $H/R_o = 1.6$. The problem is the same as the one considered in the previous section, except that a wall (grey region) is placed along the left side of the domain.

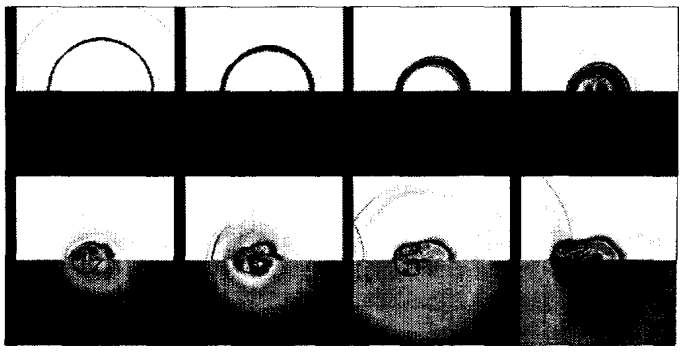

Figure 10. Numerical Schlieren and pressure contours for Rayleigh collapse near a wall, with $P/P_o = 357$ and $H/R_o = 1.6$.

In frame 1, the initial expansion is propagating radially outwards and reflects off the wall, while a shock converges to the center (frame 2). As the bubble continues to collapse in frame 3, it flattens in the direction normal to the wall [10]. The shock-wave again converges in frame 4, although this convergence is no longer spherical, due to the reflection off the now oblong bubble. The re-entrant jet is evident in frame 5 and upon hitting the distal side generates a water-hammer pressure in frame 6. This pressure wave reflects off the wall in frame 7, where the bubble now has taken the form of a vortex ring, and propagates through the bubble in frame 8. The overall behavior is similar to that of the shock-induced collapse (compare to Figure 2).

Figure 11 shows the history of the bubble volume for different initial stand-off distances. The presence of the wall retards the flow of liquid rushing to fill the void created by the collapsing bubble. As the initial stand-off distance is increased, the behavior tends to that observed during Rayleigh collapse in a free-field, *i.e.*, the collapse is more spherical. A measure of the non-sphericity of the collapse and of the prominence of the jet is provided by the difference between the maximum jet speed, v_j and the speed of the distal side, v_o, as illustrated in the cartoon of Figure 12; here, v_j is taken to be negative and v_o is positive.

The intensity of the collapse can be evaluated by considering the quantity, $v_j - v_o$; this indicates how fast the bubble walls are moving when the bubble reaches its minimum volume. A measure of non-sphericity is provided by the relative speed, $|v_j| - v_o$, which shows how much faster the jet moves than the distal side and is used to compute the water-hammer pressure in Equation 4. These values are listed in Table 2, where the results from shock-induced collapse are comparable to those obtained in the SWL problem previously studied, but in a free-field.

The most violent collapse occurs when the bubble remains

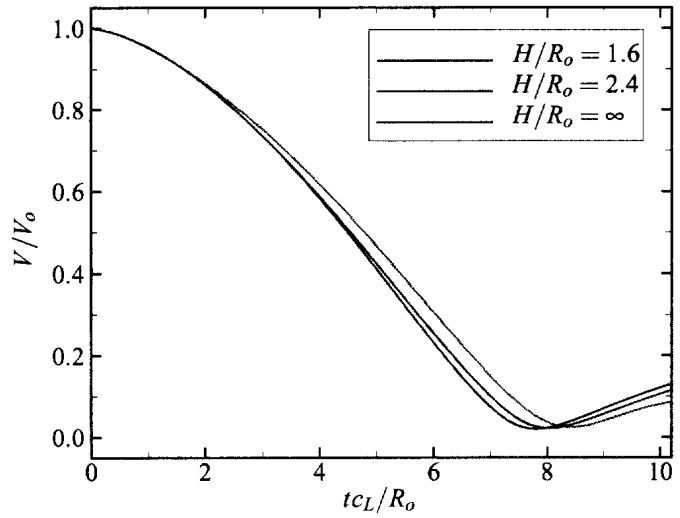

Figure 11. History of the bubble volume for different initial stand-off distances for Rayleigh collapse near a wall.

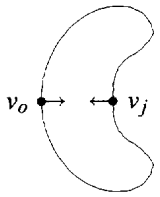

Figure 12. Jet speed and speed of the distal side.

Table 2. Difference between the jet speed and the speed fo the distal side for bubble collapse

	$v_j - v_o$	$\|v_j\| - v_o$
Shock-induced collapse	−0.36	0.14
$H/R_o = 1.6$	−0.35	0.05
$H/R_o = 2.4$	−0.38	0.03
Spherical collapse	−0.42	0.00

spherical. As the initial stand-off distance is decreased, the behavior tends to that of the shock-induced collapse. Therefore, the proximity of the wall appears to have two competing effects: retarding the bubble collapse and generating a re-entrant jet. It can be inferred that the presence of a wall in shock-induced collapse (as in the SWL problem) would enhance the re-entrant jet formation. Additional simulations are required to support this claim.

3.3 Experiments

The purpose of the experiments is to observe bubbles collapsing under lithotripsy conditions as a supplement to the numerical findings. This effort comprises observations of bubbles in a free-field geometry that are initially small ($\lesssim 1\mu$m). The bubbles are excited by a lithotripter shockwave and grow to a maximum radius of nearly 1mm. Bubble growth is then followed by a Rayleigh collapse and a rebound that can be analyzed in a fashion similar to that described by [26] for laser-initiated bubbles.

The lithotripter shockwave is generated using a Dornier HM3 clone that was developed at the University of Washington [34]. Bubble motions are then observed using both a high-speed camera (DRS Technologies, Oakland, NJ, USA) and two passive cavitation detectors (PCDs) that are aligned con-focally with the lithotripter [35]. The PCDs are spherically focused, broadband devices that can detect radiated pressures from individual bubble collapse events. With this setup, high-speed photographs are first reviewed to evaluate the density of the cavitation field, select a target bubble for analysis, and assess the symmetry of its collapse. The target bubble is then analyzed to estimate its maximum radius prior to collapse ($R_{max,1}$) and an approximate radius-time curve. The image analysis algorithm is calibrated to approximate the maximum bubble radius with an accuracy of about 2%. Finally, the bubble's collapse times are identified from the PCD data.

From these data, the Rayleigh collapse time is used to relate the measured collapse times to the maximum radius achieved during the bubble's rebound,

$$R_{max,2} = \frac{1}{0.915}\frac{t_2 - t_1}{2}\sqrt{\frac{p_\infty - p_v}{\rho_0}} \tag{7}$$

where t_1 is the time of the initial Rayleigh collapse and t_2 is the collapse after the ensuing rebound; ρ_0 is the equilibrium liquid density, p_∞ is the equilibrium pressure far from the bubble, and p_v is the vapor pressure at the ambient liquid temperature. Accordingly, the volumetric ratio $(R_{max,2}/R_{max,1})^3$ can be calculated for any observed bubble as a measure of energy retained in volumetric oscillation.

A typical sequence of the interaction between a bubble and a lithotripter pulse is shown in Figure 13. In the photographs, the bubble is backlit so that the center is bright while the edges are dark. The bubble initially grows due to the tensile part of the shockwave arriving at time zero. After reaching a maximum radius of 1.05mm, the bubble undergoes a Rayleigh collapse and a subsequent rebound. The PCDs detected an acoustic emission corresponding to this collapse at 274μs. During the rebound, a prominent jet is clearly visible despite the absence of any nearby boundaries and the visible presence of only a few small bubbles.

For test conditions with the water degassed to 10% dissolved oxygen and maintained at a temperature of 20°C, 15 indepen-

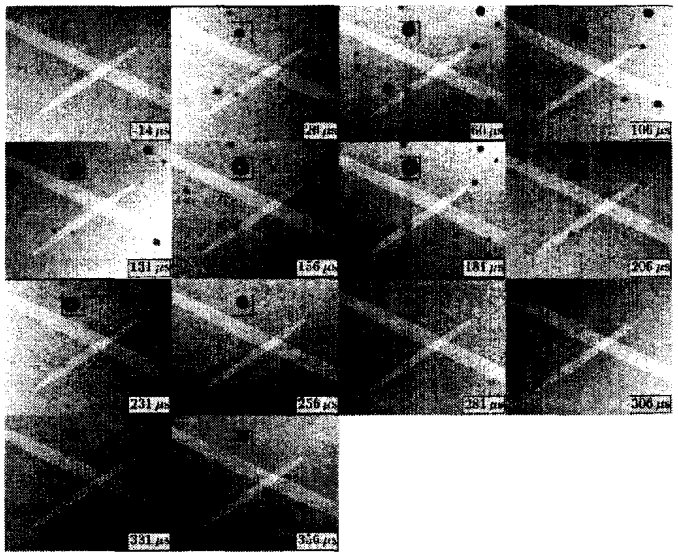

Figure 13. Sequence of high-speed photographs of a bubble excited by a lithotripter shockwave. The highlighted ellipses represent the sensitive regions of the PCDs (dimensions of smaller focal region: 17mm × 1.2mm; exposure time: 1 μs; shock arrives at time zero).

dent bubble collapses and rebounds were observed. In 10 of these bubbles, a re-entrant jet was visible during the rebound. For the remaining 5 bubbles, jets may have been present even though they were not observed with the limited temporal resolution of the photographs. The bubble rebounds analyzed here retained 3–40% of the energy present before the initial Rayleigh collapse. Note that the bubble from Figure 13 represents the top end of this range. Overall, the range of rebound energies is consistent with observations reported previously [26, 36] and, given the photographs presented by [23], the asymmetric collapses found in this work appear to correlate with wall stand-off distances, $H/R_o \gtrsim 2$. Based upon this correlation of free-field bubbles with bubbles collapsing near a wall, most of the energy dissipated during collapse can be attributed to acoustic radiation, so that a more asymmetric collapse (*i.e.*, one for which a more prominent jet forms or, in the case of collapse near a wall, for decreasing values of H/R_o) dissipates less energy in the subsequent rebounds [26]. Qualitatively, this same trend is observed here for free-field bubbles excited by a lithotripter shockwave.

Based on Figure 11, model predictions for Rayleigh collapse presented in Section 3.2 do not seem to follow the trend in dissipation versus collapse symmetry discussed above. However, the bubble conditions simulated in Section 3.2 do not accurately reflect the experimental conditions. As the model is updated to enable simulation of such conditions, tracking energy dissipation as a function of collapse symmetry may provide a useful tool for model evaluation.

4 CONCLUSIONS

Numerical simulation was used to study shock-induced and Rayleigh collapse of a gas bubble. In the case of the shock-induced collapse, it is found that the wall pressure due to the bubble collapse is much greater than that due to the incoming lithotripter pulse over the range of stand-off distance considered here. Bubbles collapsing at some distance from the wall are a potential cause of damage, while bubbles initially close to the wall and large bubbles generate very high pressures. In the case of Rayleigh collapse near a wall, preliminary results show that the proximity of the wall retards the flow and increases the prominence of the jet. Experiments show that re-entrant jets are generated in the free-field collapse of a cavitation bubble, similarly to collapse near a solid surface.

The present work provides a first step in quantifying the damage due to cavitation erosion in SWL. The next immediate steps consist in using a finer (stretched) grid and making explicit comparisons between the computations and the experiments, which are both items of on-going research. Further investigations include considerations of non-equilibrium effects (*i.e.*, expanding or collapsing bubbles) and the implementation of phase change, viscosity and surface tension. A full understanding of the non-spherical dynamics of a single bubble will allow a more appropriate study of bubble clusters in SWL and other applications.

5 ACKNOWLEDGEMENTS

This work was supported by NIH Grant PO1 DK043881 and ONR Grant N00014-06-1-0730.

REFERENCES

[1] NIH, 2004. Kidney stones in adults. On the WWW, December. URL `http://kidney.niddk.nih.gov`.

[2] Chaussy, C., 1982. *Extracorporeal Shock Wave Lithotripsy*. Karger, Basel.

[3] Lokhandwalla, M., and Sturtevant, B., 2000. "Fracture mechanics model of stone comminution in ESWL and implications for tissue damage". *Phys. Med. Biol.*, **45**, pp. 1923–1940.

[4] Zhu, S., Cocks, F. H., Preminger, G. M., and Zhong, P., 2002. "The role of stress waves and cavitation in stone comminution in shock wave lithotripsy". *Ultrasound Med. Biol.*, **28**, pp. 661–671.

[5] Coleman, A. J., Saunders, J. E., Crum, L. A., and Dyson, M., 1987. "Acoustic cavitation generated by an extracorporeal shockwave lithotripter". *Ultrasound Med. Biol.*, **13**, pp. 69–76.

[6] Crum, L. A., 1988. "Cavitation microjets as a contributory mechanism for renal calculi disintegration in ESWL". *J. Urol.*, **140**, pp. 1587–1590.

[7] Cleveland, R. O., and Sapozhnikov, O. A., 2005. "Modeling elastic wave propagation in kidney stones with application to shock wave lithotripsy". *J. Acoust. Soc. Am.*, **118**, pp. 2667–2676.

[8] Xi, X., and Zhong, P., 2001. "Dynamics photoelastic study of the transient stress field in solids during shock wave lithotripsy". *J. Acoust. Soc. Am.*, **109**, pp. 1226–1239.

[9] Pishchalnikov, Y. A., Sapozhnikov, O. A., Bailey, M. R., Williams, J. C., Cleveland, R. O., Colonius, T., Crum, L. A., Evan, A. P., and McAteer, J. A., 2003. "Cavitation bubble cluster activity in the breakage of kidney stones by lithotripter shockwaves". *J. Endourol.*, **17**, pp. 435–446.

[10] Plesset, M. S., and Chapman, R. B., 1971. "Collapse of an initially spherical vapour cavity in the neighbourhood of a solid boundary". *J. Fluid Mech.*, **47**, pp. 283–290.

[11] Philipp, A., Delius, M., Scheffczyk, C., Vogel, A., and Lauterborn, W., 1993. "Interaction of lithotripter-generated shock waves with air bubbles". *J. Acoust. Soc. Am.*, **93**, pp. 2496–2509.

[12] Ohl, C. D., and Ikink, R., 2003. "Shock-wave-induced jetting of micron-size bubbles". *Phys. Rev. Lett.*, **90**, pp. 1–4.

[13] Sankin, G. N., Simmons, W. N., Zhu, S. L., and Zhong, P., 2005. "Shock wave interaction with laser-generated single bubbles". *Phys. Rev. Lett.*, **95**, p. 034501.

[14] Johnsen, E., and Colonius, T., 2006. "Implementation of WENO schemes for compressible multicomponent flow problems". *J. Comput. Phys.*, **219**, pp. 715–732.

[15] Church, C. C., 1989. "A theoretical study of cavitation generated by an extracorporeal shock wave lithotripter". *J. Acoust. Soc. Am.*, **86**, pp. 215–227.

[16] Cocchi, J. P., Saurel, R., and Loraud, J. C., 1996. "Treatment of interface problems with Godunov-type schemes". *Shock Waves*, **5**, pp. 347–357.

[17] Harlow, F., and Amsden, A., 1971. Fluid dynamics. Tech. Rep. LANL Monograph LA-4700, Los Alamos National Labs.

[18] Ding, Z., and Gracewski, S. M., 1996. "The behaviour of a gas cavity impacted by a weak or strong shock wave". *J. Fluid Mech.*, **309**, pp. 183–209.

[19] Ball, G. J., Howell, B. P., Leighton, T. G., and Schofield, M. J., 2000. "Shock-induced collapse of cylindrical air cavity in water: Free-lagrange simulation". *Shock Waves*, **10**, pp. 265–276.

[20] Bourne, N. K., and Field, J. E., 1992. "Shock-induced collapse of single cavities in liquids". *J. Fluid Mech.*, **244**, pp. 225–240.

[21] Klaseboer, E., Turangan, C., Fong, S. W., Liu, T. G., Hung, K. C., and Khoo, B. C., 2006. "Simulations of pressure pulse-bubble interaction using boundary element method". *Comput. Methods Appl. Mech. Engrg.*, **195**, pp. 4287–4302.

[22] Quirk, J. J., and Karni, S., 1996. "On the dynamics of a shock-bubble interaction". *J. Fluid Mech.*, **318**, pp. 129–163.

[23] Vogel, A., Lauterborn, W., and Timm, R., 1989. "Optical and acoustic investigations of the dynamics of laser-produced cavitation bubbles near a solid boundary". *J. Fluid Mech.*, **206**, pp. 299–338.

[24] Haas, J. F., and Sturtevant, B., 1987. "Interaction of weak shock waves with cylindrical and spherical gas inhomogeneities". *J. Fluid Mech.*, **181**, pp. 41–76.

[25] Best, J. P., 1993. "The formation of toroidal bubbles upon the collapse of transient cavities". *J. Fluid Mech.*, **251**, pp. 79–107.

[26] Vogel, A., and Lauterborn, W., 1988. "Acoustic transient generation by laser-produced cavitation bubbles near solid boundaries". *J. Acoust. Soc. Am.*, **84**, pp. 719–731.

[27] Johnsen, E., and Colonius, T., 2006. "Computations of shock-bubble interaction and aspherical bubble collapse". In Proceedings of the Sixth International Symposium on Cavitation (CAV2006), Wageningen, Netherlands.

[28] Kameda, M., Shimaura, N., Higashino, F., and Matsumoto, Y., 1998. "Shock waves in a uniform bubbly flow". *Phys. Fluids*, **10**, pp. 2661–2668.

[29] Rayleigh, L., 1917. "On the pressure developed in a liquid during the collapse of a spherical cavity". *Phil. Mag.*, **34**, pp. 94–98.

[30] Plesset, M. S., and Mitchell, T. P., 1956. "On the stability of the spherical shape of a vapor cavity in a liquid". *Quart. Appl. Math.*, **13**, pp. 419–430.

[31] Cole, R., 1948. *Underwater Explosions*. Princeton University Press, Princeton, NJ.

[32] Ohl, C. D., Kurz, T., Geisler, R., Lindau, O., and Lauterborn, W., 1999. "Bubble dynamics, shock waves and sonoluminescence". *Phil. Trans. R. Soc. Lond. A*, **357**, pp. 269–294.

[33] Gilmore, F. R., 1952. The growth and collapse of a spherical bubble in a viscous compressible liquid. Tech. Rep. Rep. 26-4, Calif. Inst. Technol. Eng. Div.

[34] Cleveland, R. O., Bailey, M. R., Fineberg, N., Hartenbaum, B., Lokhandwalla, M., McAteer, J. A., and Sturtevant, B., 2000. "Design and characterization of a research electrohydraulic lithotripter patterned after the Dornier HM3". *Rev. Sci. Instrum.*, **71**, pp. 2514–2525.

[35] Kreider, W., Crum, L. A., Bailey, M. R., Matula, T. J., Khokhlova, V. A., and Sapozhnikov, O. A., 2006. "Acoustic cavitation and medical ultrasound". In Proceedings of the Sixth International Symposium on Cavitation (CAV2006), Wageningen, Netherlands.

[36] Akhatov, I., Lindau, O., Topolnikov, A., Mettin, R., Vakhitova, N., and Lauterborn, W., 2001. "Collapse and rebound of a laser-induced cavitation bubble". *Phys. Fluids*, **13**, pp. 2805–2819.